OPTICS

Tailoring excitonic states of van der Waals bilayers through stacking configuration, band alignment, and valley spin

Wei-Ting Hsu[1], Bo-Han Lin[2], Li-Syuan Lu[2], Ming-Hao Lee[3], Ming-Wen Chu[3], Lain-Jong Li[4,5], Wang Yao[6]*, Wen-Hao Chang[2,7]*, Chih-Kang Shih[1]*

Excitons in monolayer semiconductors have a large optical transition dipole for strong coupling with light. Interlayer excitons in heterobilayers feature a large electric dipole that enables strong coupling with an electric field and exciton-exciton interaction at the cost of a small optical dipole. We demonstrate the ability to create a new class of excitons in hetero- and homobilayers that combines advantages of monolayer and interlayer excitons, i.e., featuring both large optical and electric dipoles. These excitons consist of an electron confined in an individual layer, and a hole extended in both layers, where the carrier-species–dependent layer hybridization can be controlled through rotational, translational, band offset, and valley-spin degrees of freedom. We observe different species of layer-hybridized valley excitons, which can be used for realizing strongly interacting polaritonic gases and optical quantum controls of bidirectional interlayer carrier transfer.

INTRODUCTION

Van der Waals (vdW) bilayers composed of stacking two atomically thin two-dimensional (2D) layers have rapidly evolved into a variety of designer quantum materials with many fascinating properties that are not possessed by the constituent monolayers (*1*–*12*). The key control knob for designing new quantum materials is the stacking-dependent interlayer coupling, which determines the electronic structure of the vdW bilayer as a whole. One strategy is to harness the “moiré pattern”—a periodic variation of local stacking configuration (due to twist angle and/or lattice mismatch)—to form a 2D electronic superlattice. Such a moiré designer has led to the observation of the Mott insulating phase and, more intriguingly, the accompanying unconventional superconductivity in twisted bilayer graphene (*13*, *14*). In semiconducting transition metal dichalcogenide (TMD) heterobilayers, this strategy has also been used to create interlayer moiré excitons, which have attractive properties such as tunable quantum emitters and spin-orbit–coupled superlattice (*12*, *15*–*18*). While the formation of the moiré exciton has been stated, an in situ structural confirmation is still needed to directly connect the observed excitonic features to the formation of excitonic moiré superlattice in the experiments (*15*–*18*).

Here, we report structural and spectroscopic evidence that coherently shows how stacking configurations, band alignment, and valley-specific spin configurations work in concert to define the excitonic structures of the vdW bilayers. More specifically, using the above degrees of freedom, we tailor different species of layer-hybridized excitonic states in TMD hetero- and homobilayers that feature both a large optical dipole (comparable to that of monolayer exciton) and a large electric dipole (comparable to that of interlayer exciton), which are highly desired for realizing strongly interacting excitonic/polaritonic gases and can also be exploited for spin valley–selective interlayer quantum controls. In addition, we determine quantitatively important coupling parameters for future design of electronic structures of vdW bilayers.

RESULTS AND DISCUSSION

The layer hybridization of electronic states in bilayers can be described by a two-level Hamiltonian: $\begin{bmatrix}\varepsilon_u & -t\\ -t & \varepsilon_l\end{bmatrix}$ (Fig. 1A), where the basis states $|\psi_u\rangle$ and $|\psi_l\rangle$ are the states from upper and lower layers before coupling. The off-diagonal element t is the interlayer hopping integral that conserves the spin. For the electronic states at the $\pm K$ valleys, the hopping integral t is strongly dependent on the stacking configuration (*11*). Noticeably at high-symmetry stacking, threefold rotational symmetry dictates t to be zero/finite at certain band edges, where interlayer hybridization is forbidden/allowed (c.f. Fig. 1, B to F). On the other hand, the offset $2\delta = \varepsilon_l - \varepsilon_u$ between the band edges from the two layers is controlled by valley-spin splitting together with the valley pairing that is opposite in the R- and H-type stackings. The two layer-hybridized eigen vectors are $|\psi_{h+}\rangle = \alpha|\psi_u\rangle + \beta|\psi_l\rangle$ and $|\psi_{h-}\rangle = \alpha'|\psi_u\rangle + \beta'|\psi_l\rangle$, where $\beta/\alpha = t/(\delta - \Delta)$, $\beta'/\alpha' = t/(\delta + \Delta)$, and $\Delta = \sqrt{\delta^2 + t^2}$. The energy separation between the doublet is 2Δ, which, together with the spectral ratio $|\beta/\alpha|^2$, can provide signature of the hybridization. The degree of layer hybridization is further defined as $P_H = |\beta/\alpha|$.

Our vdW bilayer samples include $WSe_2/MoSe_2$ and WS_2/MoS_2 heterobilayers with negligible lattice mismatch, and MoS_2 homobilayers grown directly by chemical vapor deposition (CVD) (*10*). The fundamental characterizations can be found in figs. S1 to S3. Despite a slight lattice mismatch of ~0.2 to 0.4% between WX_2 and MoX_2 (X = S, Se), the top layer of the CVD-grown WX_2/MoX_2 heterobilayers tends to adopt the same lattice constant as the bottom layer (fig. S4) to form commensurate R (twist angle $\theta = 0°$) and H stacking

---

[1]Department of Physics, The University of Texas at Austin, Austin, TX 78712, USA. [2]Department of Electrophysics, National Chiao Tung University, Hsinchu 30010, Taiwan. [3]Center for Condensed Matter Sciences, National Taiwan University, Taipei 10617, Taiwan. [4]Physical Sciences and Engineering Division, King Abdullah University of Science and Technology, Thuwal, Jeddah 23955-6900, Kingdom of Saudi Arabia. [5]School of Materials Science and Engineering, University of New South Wales, Sydney 2052, Australia. [6]Department of Physics and Center of Theoretical and Computational Physics, The University of Hong Kong, Hong Kong, China. [7]Center for Emergent Functional Matter Science (CEFMS), National Chiao Tung University, Hsinchu 30010, Taiwan.
*Corresponding author. Email: shih@physics.utexas.edu (C.-K.S.); whchang@mail.nctu.edu.tw (W.-H.C.); wangyao@hku.hk (W.Y.)

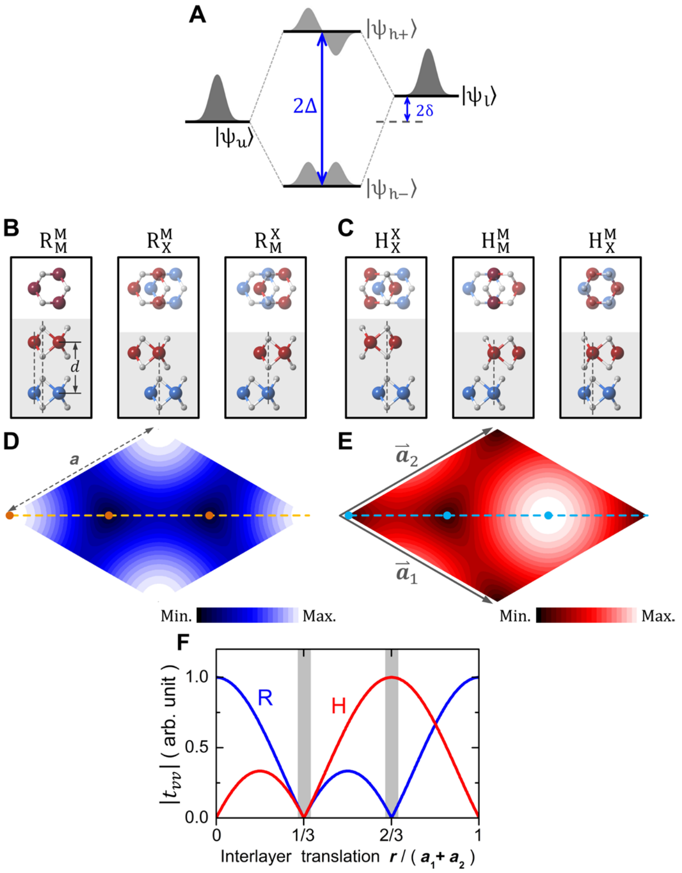

Fig. 1. Interlayer hybridization of valence bands at K valleys for commensurate TMD heterobilayer. (**A**) Schematic showing the hybridization of electronic states from upper ($|\psi_u\rangle$) and lower ($|\psi_l\rangle$) layers. (**B** and **C**) High-symmetry R-type (B) and H-type (C) stacking configurations, where the top (side) view is shown in the upper (lower) panel. R^μ_ν (H^μ_ν) denotes an R-type (H-type) stacking with μ sites of the upper layer vertically aligned with ν sites of the lower layer, where μ, ν = M or X. (**D** and **E**) The interlayer hopping integral $|t_{vv}|$ as a function of interlayer translation **r** for R-type (D) and H-type (E) heterobilayers, where the dots correspond to the high-symmetry stacking configurations shown in (B) and (C), respectively. (**F**) $|t_{vv}|$ of R-type (blue) and H-type (red) heterobilayers along the dashed diagonal line are shown for comparison.

(θ = 60°), as schematically shown in Fig. 1 (B and C). The interlayer atomic registry has been examined by transmission electron microscopy (TEM). Only the H^M_X stacking configuration was observed in H stacking samples. TEM inspections on different locations of the same sample also confirm that the stacking has no interlayer translation (*10*). In R stacking samples, only the R^M_X or R^X_M stacking configurations were observed (Fig. 2, A and B). According to Fig. 1F, the hopping integral reaches the maximum in H^M_X stacking but vanishes in R^M_X and R^X_M stacking configurations.

The stacking-dependent interlayer coupling, the band alignment, and the valley-spin work collaboratively to determine the hybridization of electronic states at *K* point, leading to rich excitonic structures. Shown in Fig. 2C are the differential reflectance (DR) spectra acquired at 4 K for a H^M_X-stacked and a R^X_M-stacked $WSe_2/MoSe_2$ heterobilayer. The most notable difference emerges from the B exciton of WSe_2 (denoted as X^W_B), which shows a single peak in R stacking, but becomes a doublet (referred to as X^W_{h+} and X^W_{h-}) in H stacking with a splitting of 92 meV and a spectral weight ratio of roughly 1:1. In addition, the oscillator strength of the X^{Mo}_A (X^W_A) excitons is reduced (enhanced) in H stacking. This can be explained by the splitting of the X^{Mo}_A exciton peak into a doublet (X^{Mo}_{h+} and X^{Mo}_{h-}), where the split-off spectral feature merges with the X^W_A excitons. Curve fitting yields a splitting of 87 meV and a spectral weight ratio of nearly 1:1. These spectral features can be further enhanced by taking the second derivative of these spectra, as displayed in Fig. 2C. The measurements have been carried out on several samples with well-defined R or H stacking. In all cases, the H^M_X-stacked heterobilayers exhibit spectral splitting in X^W_B, albeit the splitting varies from 70 to 105 meV (fig. S5). In Fig. 2D, we show an example of spectral fitting for an H-type heterobilayer.

The $WSe_2/MoSe_2$ heterobilayer is known to exhibit a type II band alignment, where the valence band maximum of WSe_2 is lying above that of $MoSe_2$, as schematically shown in Fig. 2E. We label the two valence bands split by spin-orbit coupling (SOC) as v1 and v2 for WSe_2, and v1′ and v2′ for $MoSe_2$. Because of the larger SOC splitting in WSe_2 and the type II alignment, the v2 band aligns closer to the v1′ and v2′ bands of $MoSe_2$ (*19*). Spin conservation of interlayer hopping, on the other hand, ensures that the v2 band of WSe_2 only coupled to the v1′ band of $MoSe_2$ in H stacking (Fig. 2E). Such a coupling hybridizes v2 and v1′ bands into the doublet h+ and h−, as depicted in Fig. 2E. Conduction band hybridization, however, is not allowed in this high-symmetry stacking (*11*). Interband optical transition can excite either of the hybridized valance states (h+ and h−) to the conduction band localized in the WSe_2 ($MoSe_2$) layer, leading to the splitting of the X^W_B (X^{Mo}_A) exciton state into a doublet X^W_{h+} and X^W_{h-} (X^{Mo}_{h+} and X^{Mo}_{h-}) as shown in Fig. 2E. These four exciton species, all consisting of a layer-hybridized hole and an electron confined in an individual layer (Fig. 2F), feature a large optical dipole that is one-half of the monolayer exciton one and a large electric dipole in the out-of-plane direction. They, therefore, combine the advantage of both intralayer excitons (for strong light coupling) and interlayer excitons (for electric tunability of resonances and strong dipole-dipole interaction).

According to the coupled two-level model, the band offset 2δ and the hopping integral *t* can be deduced from the measured energy splitting ($2\sqrt{\delta^2 + t^2}$) and the spectral weight ratio ($|\beta/\alpha|^2$). Measurements conducted on several samples show that the spectral weight ratio is in the range of 1.1 to 1.5, and the splitting ranges from 70 to 105 meV, which determines a hopping integral of $t_{vv} = 43 \pm 9$ meV and a band offset of $2\delta = 12 \pm 2$ meV between the v2 and v1′ bands. We, thus, obtained a very high degree of layer hybridization of $P_H \approx 87\%$ for holes. We have also performed temperature-dependent measurements from 4 to 300 K. We found that the splitting and spectral ratio are temperature independent, indicating that the band offset and interlayer hopping integral remain invariant in this temperature range (fig. S6).

The layer-hybridized excitonic states further enable the possibility of interlayer quantum control. As depicted in Fig. 2 (E and G), the excitonic transitions form a three-level Λ-system that would allow the interlayer quantum control of electrons via the layer-hybridized holes. The schematic shown in Fig. 2G is an example of two states with a layer-confined electron in the $MoSe_2$ ($|\psi^{Mo}_e\rangle$) and the WSe_2 ($|\psi^W_e\rangle$) layers, which can be connected by an intermediate state of interlayer negative trion (IX^-) through optical excitations. Considering the initial state $|\psi^{Mo}_e\rangle$ (i.e., an electron in the $MoSe_2$ layer), the IX^- can be created by a π-pulse resonant excitation of X^W_{h+}. By using another

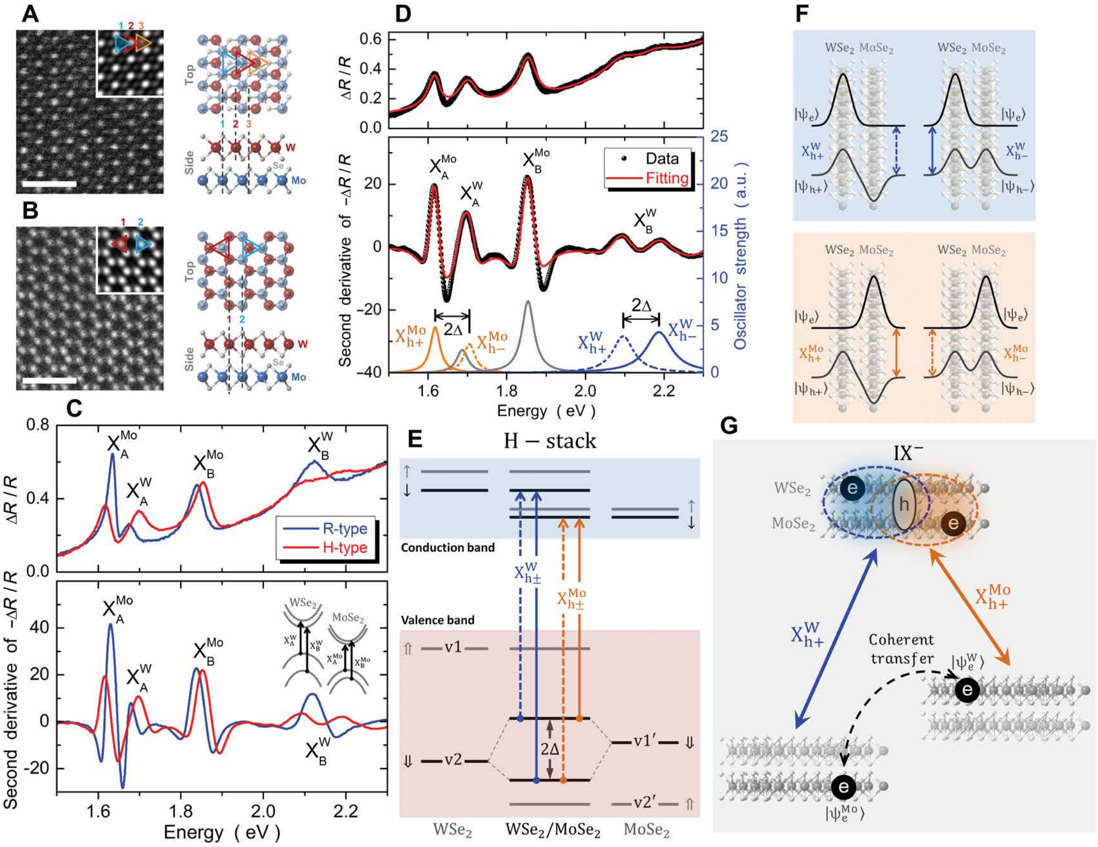

Fig. 2. Layer-hybridized valley excitons in the WSe$_2$/MoSe$_2$ heterobilayer. (**A** and **B**) TEM and Bragg-filtered (inset) images of R_M^X (A) and H_X^M (B) heterobilayers. The ideal atomic registry is illustrated for comparison, where the top (side) view is shown in the upper (lower) panel. Scale bars, 1 nm. (**C**) The differential reflectance (DR; upper panel) and second derivative (lower panel) spectra of an R_M^X (blue curves) and an H_X^M (red curves) heterobilayer, showing a clear splitting of X_B^W for the H_X^M heterobilayer. (**D**) The DR (upper panel) and second derivative (lower panel) spectra of an H_X^M heterobilayer shown with the spectra fitting (red curve). (**E**) Schematic showing the optical transitions of the H_X^M heterobilayer at K valley. Note that both X_B^W (blue) and X_A^{Mo} (orange) transitions are split into two hybridized transitions ($X_{h\pm}^W$ and $X_{h\pm}^{Mo}$), corresponding to the fitting curves in (D). The transitions form Λ-shape level schemes that allow the interlayer quantum control of electrons. (**F**) Schematics showing the wave functions in the out-of-plane direction for the four species of layer-hybridized valley excitons, featuring both large optical dipoles and large electric dipoles compared with that of monolayer and interlayer excitons. (**G**) A schematic showing the spin valley–selective interlayer quantum control of electron states by $X_{h\pm}^W$ and $X_{h\pm}^{Mo}$ transitions intermediated via an interlayer negative trion IX$^-$. a.u., arbitrary units.

π-pulse excitation in resonance with X_{h+}^{Mo}, the trion state will be forced to recombine, leaving behind the final state $|\psi_e^W\rangle$ (i.e., an electron in the WSe$_2$ layer). Note that this quantum control process is bidirectional with spin-valley selectivity through helicity-dependent optical excitations.

Similar interlayer hybridization has also been observed in WS$_2$/MoS$_2$ heterobilayers at room temperature. For this sample set, we also performed measurements on samples with different twist angles. We have identified several commensurate heterobilayers with the R_M^X, R_X^M, and H_X^M stacking configurations based on TEM analyses (Fig. 3, A to C), and some twisted bilayers using second harmonic generation (SHG) microscopy. Figure 3D shows the second derivative spectra for heterobilayers with different twist angles. The doublet of the X_B^W exciton is observed only for θ = 60° (H stacking). The splitting is smaller (74 ± 6 meV for the spectrum shown in Fig. 3E) than that of the WSe$_2$/MoSe$_2$ heterobilayers, indicative of a weaker interlayer hopping in WS$_2$/MoS$_2$ heterobilayers. From the measured splitting and fitted spectral weight, we determine the interlayer hopping to be $t_{vv} = 36 \pm 4$ meV, band offset $2\delta = -7 \pm 20$ meV, and $P_H \approx 90\%$ in WS$_2$/MoS$_2$ heterobilayers. For the R_M^X and R_X^M heterobilayers (Figs. 1F and 3, A and B), layer-hybridized valley excitons are absent since the interlayer hopping is dictated to be 0 for both the conduction and valance band edges. On the other hand, the absence of interlayer hybridization at the K point in twisted bilayers can be understood from two factors. First, the K valleys of the two layers in momentum space are misaligned by the twist angle θ (Fig. 3D, inset), where the interlayer hopping is inhibited by the large momentum mismatch. Second, since the interlayer hopping decreases exponentially with the interlayer spacing d, the enlarged interlayer spacing in twisted heterobilayers, thus, further suppresses the interlayer hopping (*20*–*23*). Nevertheless, the interlayer hybridization of the Γ and Q points in twisted bilayers is also possible and has been reported previously (*24*, *25*).

The H_X^M heterobilayers demonstrated above exemplify the interlayer hybridization in the regime with $t > \delta$. The R_M^X and R_X^M heterobilayers, on the other hand, represent the example of vanished

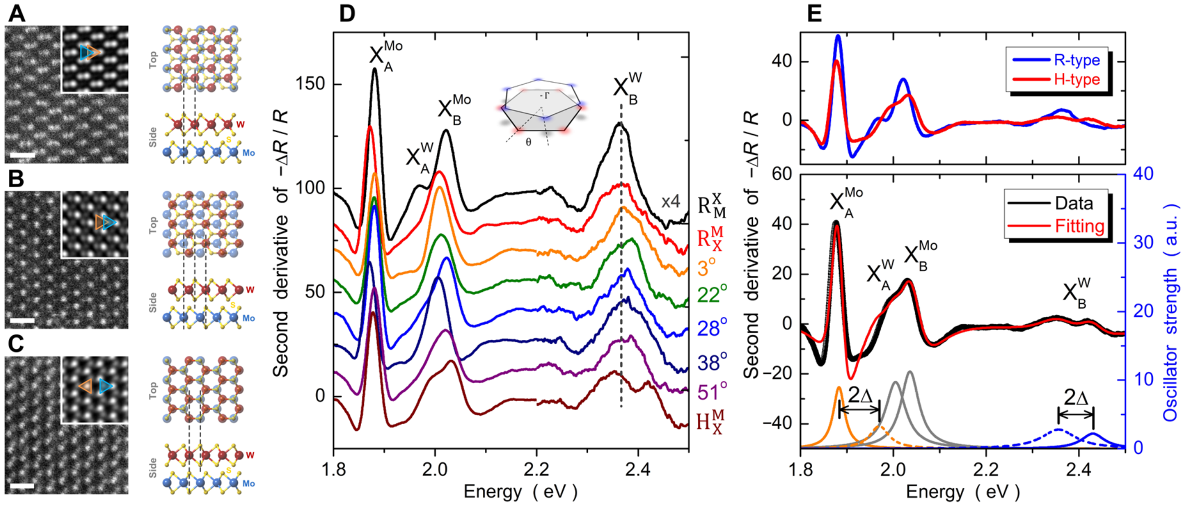

Fig. 3. Layer-hybridized valley excitons in the WS$_2$/MoS$_2$ heterobilayer. (**A** to **C**) TEM and Bragg-filtered (inset) images of R_M^X (A), R_X^M (B), and H_X^M (C) heterobilayers. The ideal atomic registry is illustrated for comparison, where the top (side) view is shown in the upper (lower) panel. Scale bars, 0.5 nm. (**D**) The second derivative spectra as a function of twist angle θ. Only the H_X^M heterobilayer exhibits interlayer hybridization. (**E**) A comparison of R_M^X and H_X^M heterobilayers (upper panel), showing a clear splitting of X_B^W for the H_X^M heterobilayer. The second derivative spectrum (lower panel) of the H_X^M heterobilayer with spectral fitting (red curve).

interlayer hopping $t = 0$ (*11*). In principle, one can tune the band offset 2δ by a vertical electric field to tune the degree of hybridization (*26*). However, fabricating the device to achieve such tunability is not straightforward, especially when the heterobilayer area is small. Here, we show that H-stacked MoS$_2$ homobilayers can be a model system to investigate the interlayer hybridization of valance bands in the regime with $\delta > t$. The MoS$_2$ bilayers investigated here include commensurate R_M^X- and H_X^M stacking and twisted bilayers, as characterized by TEM and SHG measurements (fig. S7). Figure 4A shows the second derivative spectra for bilayer MoS$_2$ as a function of θ, showing A-exciton (X_A^{Mo}) and B-exciton (X_B^{Mo}) transitions in all samples. Because of the small spin splitting in the conduction band of MoS$_2$, the energy splitting between X_A^{Mo} and X_B^{Mo} thus represents a good measure of the valence band spin splitting at the K valley. As depicted in Fig. 4B, the A-B exciton splitting for R_M^X and twisted bilayers are around 144 meV, which is very close to the value of 148 meV for monolayer MoS$_2$ and insensitive to the twist angle. The slightly reduced energy splitting in bilayers could be caused by the enhanced dielectric screening. On the contrary, the energy splitting of the H_X^M bilayer is increased to 164 meV. The same A-B exciton separation between twisted and R_M^X bilayers is a confirmation on the absence of interlayer hybridization in the R_M^X bilayer, as discussed above. On the other hand, the enlarged energy splitting indicates the presence of partial interlayer hybridization in the H_X^M homobilayer. Figure 4C depicts the optical transitions at the K valley of the H-type bilayer. Here, we denote the valence band spin splitting of monolayer MoS$_2$ as 2λ. The presence (absence) of interlayer hopping t thus modifies the spin splitting to $2\sqrt{\lambda^2 + t^2}$ (2λ) for the H_X^M (R_M^X) bilayer. Comparing the A-B exciton separation in H_X^M bilayers and in twisted bilayers without interlayer hopping, we determine the interlayer hopping integral in the MoS$_2$ bilayer to be $t_{vv} = 39$ meV, which is close to the theoretical calculation (*6*) and similar to those for the WX$_2$/MX$_2$ heterobilayers. From the measured λ and t, the degree of layer hybridization of hole is obtained to be $P_H \approx 26\%$, which is much smaller than that of heterobilayers and forms a partially layer-hybridized hole.

We note the fact that, in bilayer MoS$_2$, the interlayer hybridization enables a total of eight transitions of partially layer-hybridized valley excitons as shown in Fig. 4 (D to E), with both spin-up and spin-down holes becoming relevant in each valley. Four of them X_h^o have large optical dipoles (~97% compared with that of monolayer exciton) and moderate electric dipoles (~25% compared with that of interlayer exciton). The other four X_h^e have large electric dipoles (~97% compared with that of interlayer exciton) and moderate optical dipoles (~25% compared with that of monolayer exciton). The X_h^o and X_h^e exciton transition energies differ by the conduction band spin splitting, not resolvable here due to the small splitting in MoS$_2$ (~3 meV), while the much larger splitting in other TMDs shall allow separate access of these exciton states. Two Λ-shape level schemes are enabled in the spin-up and spin-down subspaces, respectively, by these layer-hybridized excitons, allowing the interlayer quantum control of both spin species in each valley.

CONCLUSION

Our work has demonstrated the first observation of the interlayer hybridization of K valleys in TMD hetero- and homobilayers, which is consistent with the symmetry-dictated registry dependence. The interlayer hopping integral of the valence band is determined to be $t_{vv} \approx 36$ to 43 meV, depending on the material combinations. While most research has focused on the band-edge moiré excitons in TMD heterobilayers, the obtained interlayer hopping strength at high-symmetry points provides a measure for the upper limit of confinement potential in a TMD-based moiré superlattice. By using the interlayer hybridization, creating a moiré potential up to ~100 meV becomes feasible in TMD hetero- and homobilayers. Moreover, our work points out a more notable moiré modulation effect in electronic structures, where the layer distribution of out-of-plane

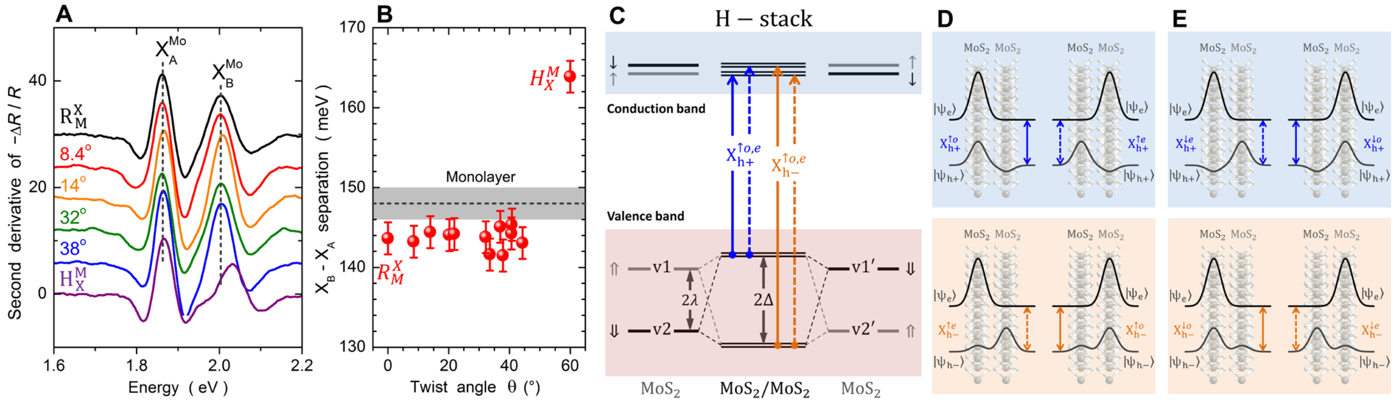

Fig. 4. Partially layer-hybridized valley excitons in bilayer MoS$_2$. (**A**) The second derivative spectra of bilayer MoS$_2$ as a function of twist angle θ. (**B**) The energy separation between X_A^{Mo} and X_B^{Mo} as a function of θ, where the H_X^M bilayer is a singular point featuring a separation larger by ~20 meV. (**C**) Schematic showing the optical transitions of spin-up excitons in the H_X^M heterobilayer at K valleys, where both X_A^{Mo} and X_B^{Mo} transitions are split into hybridized transitions ($X_{h+}^{\uparrow o,e}$ and $X_{h-}^{\uparrow o,e}$). Note that the valence band spin splitting in the H_X^M bilayer is increased from 2λ to $2\sqrt{\lambda^2 + t^2}$ by the presence of finite interlayer hopping (t), whereas in the R_M^X bilayer, the interlayer hybridization is absent by symmetry. (**D** and **E**) Schematics showing the wave functions in the out-of-plane direction for the eight species of partially layer-hybridized excitons per valley with spin up (D) and spin down (E). Note four of them X_h^o have large optical dipoles (moderate electric dipoles) of ~97% (~25%) compared with that of monolayer (interlayer) exciton. The other four X_h^e have large electric dipoles (moderate optical dipoles) of ~97% (~25%) compared with that of interlayer (monolayer) exciton.

wave function can strongly depend on in-plane locations in the moiré. It can become a brand new control knob to engineer excitons in the bilayer, paving the way toward the next-generation artificial platform for exploring exciton physics and engineering moiré quantum dot arrays. In addition, the layer-hybridized valley excitons can be used for realizing strongly interacting excitonic/polaritonic gases, as well as spin valley–selective optical quantum coherent controls of bidirectional interlayer carrier transfer with either upper conversion or down conversion in energy.

MATERIALS AND METHODS

Growth of bilayer TMD heterostructures and homostructures

Single-crystal WSe$_2$/MoSe$_2$ heterobilayers, WS$_2$/MoS$_2$ heterobilayers, and MoS$_2$ homobilayers were grown on sapphire substrates in a horizontal hot-wall CVD chamber using the one-pot synthesis process (*27*, *28*). The high-purity WO$_3$ (99.995%, Aldrich), MoO$_2$ (99%, Aldrich), Se (99.5%, Alfa), and S (99%, Aldrich) powders were used as the source precursors. The sapphire substrate and metal-oxide powder were placed at the central heating zone, while the chalcogen powder was heated by a heating belt at the upstream end. For WSe$_2$/MoSe$_2$ heterobilayers, the heterostructures were grown at 880°C in Ar/H$_2$ flowing gas with flow rates of 60/6 sccm at low pressure (5 to 40 Torr) (*10*). For WS$_2$/MoS$_2$ heterobilayers, the growth temperature was set to 920°C in Ar/H$_2$ flowing gas with flow rates of 60/6 sccm at low-pressure conditions (5 Torr). The MoS$_2$ homobilayers were grown at 650°C in Ar flowing gas at ambient pressure.

TEM characterizations

Annular dark-field scanning TEM imaging was performed in a spherical aberration-corrected TEM (JEOL-2100F). The CVD-grown samples were transferred onto the TEM grids using the conventional wet-transfer process. The TMD/sapphire samples were capped with a layer of poly(methylmethacrylate) (PMMA) (950K A4) by spin coating, followed by baking at 100°C for 60 min. The PMMA-capped sample was then immersed into a buffered oxide etch (BOE) solution at 80°C for 20 min. After diluting etchant and residues in deionized water, the PMMA film was exfoliated from the sapphire substrate and transferred onto a Cu grid with carbon nets (Ted Pella). Then, the top PMMA film was removed by acetone, and the sample was cleaned by isopropyl alcohol and deionized water.

Optical measurements

Room temperature optical characterizations, such as photoluminescence (PL), Raman, and SHG spectroscopies, were performed using a back-scattering optical microscope. The light sources were focused on the sample by a 100× objective lens [numerical aperture (NA), 0.9], and the signal was sent to a 0.75-m monochromator and then detected by a nitrogen-cooled charge-coupled device camera. For PL and Raman measurements, a 532-nm solid-state laser was used as the excitation source. For SHG measurements, the fundamental laser field was provided by a mode-locked Ti:sapphire laser at 880 nm. The polarization of the fundamental laser (SHG signal) was selected (analyzed) by the individual linear polarizers and half-wave plates (*29*).

For low-temperature DR measurements, the sample was cooled down to $T = 4$ K by a cryogen-free low-vibration cryostat equipped with a three-axis piezo positioner and a 50× objective lens (NA, 0.82). A fiber-coupled tungsten halogen lamp was used as the light source. To improve the spatial resolution, the confocal optics were set up in front of the monochromator, resulting in a final spatial resolution of ~0.5 μm. The integration time per spectrum was around 4 s, where the signal-to-noise ratio was further improved by averaging >100 spectra. The second derivative spectra were numerically smoothed using the Savitzky-Golay method, resulting in an overall energy resolution of ~5 meV.

SUPPLEMENTARY MATERIALS

Supplementary material for this article is available at http://advances.sciencemag.org/cgi/content/full/5/12/eaax7407/DC1

Fig. S1. Room temperature characterizations of $WSe_2/MoSe_2$ heterobilayers by Raman and PL spectroscopies.
Fig. S2. Room temperature characterizations of WS_2/MoS_2 heterobilayers by Raman and PL spectroscopies.
Fig. S3. Room temperature characterizations of MoS_2 homobilayers by Raman and PL spectroscopies.
Fig. S4. Strain effect of commensurate $WSe_2/MoSe_2$ heterobilayers.
Fig. S5. Optical transitions of H_X^M $WSe_2/MoSe_2$ heterobilayer.
Fig. S6. Temperature-dependent DR spectra of H_X^M $WSe_2/MoSe_2$ heterobilayer.
Fig. S7. TEM characterizations of bilayer MoS_2.
Fig. S8. Low-temperature PL of $WSe_2/MoSe_2$ heterobilayer with R-type and H-type stackings.
Fig. S9. Scanning TEM images at different locations of $WSe_2/MoSe_2$ heterobilayer with R-type and H-type stackings.
Fig. S10. DR spectrum of WS_2/MoS_2 heterobilayer with H-type stacking.
Note S1. Low-temperature PL measurements.
References (*30*–*33*)

REFERENCES AND NOTES

1. A. K. Geim, I. V. Grigorieva, Van der Waals heterostructures. *Nature* **499**, 419–425 (2013).
2. L. A. Ponomarenko, R. V. Gorbachev, G. L. Yu, D. C. Elias, R. Jalil, A. A. Patel, A. Mishchenko, A. S. Mayorov, C. R. Woods, J. R. Wallbank, M. Mucha-Kruczynski, B. A. Piot, M. Potemski, I. V. Grigorieva, K. S. Novoselov, F. Guinea, V. I. Fal'ko, A. K. Geim, Cloning of Dirac fermions in graphene superlattices. *Nature* **497**, 594–597 (2013).
3. C. R. Dean, L. Wang, P. Maher, C. Forsythe, F. Ghahari, Y. Gao, J. Katoch, M. Ishigami, P. Moon, M. Koshino, T. Taniguchi, K. Watanabe, K. L. Shepard, J. Hone, P. Kim, Hofstadter's butterfly and the fractal quantum Hall effect in moiré superlattices. *Nature* **497**, 598–602 (2013).
4. B. Hunt, J. D. Sanchez-Yamagishi, A. F. Young, M. Yankowitz, B. J. LeRoy, K. Watanabe, T. Taniguchi, P. Moon, M. Koshino, P. Jarillo-Herrero, R. C. Ashoori, Massive Dirac fermions and Hofstadter butterfly in a van der Waals heterostructure. *Science* **340**, 1427–1430 (2013).
5. R. V. Gorbachev, J. C. W. Song, G. L. Yu, A. V. Kretinin, F. Withers, Y. Cao, A. Mishchenko, I. V. Grigorieva, K. S. Novoselov, L. S. Levitov, A. K. Geim, Detecting topological currents in graphene superlattices. *Science* **346**, 448–451 (2014).
6. Z. Gong, G.-B. Liu, H. Yu, D. Xiao, X. Cui, X. Xu, W. Yao, Magnetoelectric effects and valley-controlled spin quantum gates in transition metal dichalcogenide bilayers. *Nat. Commun.* **4**, 2053 (2013).
7. M. M. Fogler, L. V. Butov, K. S. Novoselov, High-temperature superfluidity with indirect excitons in van der Waals heterostructures. *Nat. Commun.* **5**, 4555 (2014).
8. H. Yu, Y. Wang, Q. Tong, X. Xu, W. Yao, Anomalous light cones and valley optical selection rules of interlayer excitons in twisted heterobilayers. *Phys. Rev. Lett.* **115**, 187002 (2015).
9. P. Rivera, K. L. Seyler, H. Yu, J. R. Schaibley, J. Yan, D. G. Mandrus, W. Yao, X. Xu, Valley-polarized exciton dynamics in a 2D semiconductor heterostructure. *Science* **351**, 688–691 (2016).
10. W.-T. Hsu, L.-S. Lu, P.-H. Wu, M.-H. Lee, P.-J. Chen, P.-Y. Wu, Y.-C. Chou, H.-T. Jeng, L.-J. Li, M.-W. Chu, W.-H. Chang, Negative circular polarization emissions from $WSe_2/MoSe_2$ commensurate heterobilayers. *Nat. Commun.* **9**, 1356 (2018).
11. Q. Tong, H. Yu, Q. Zhu, Y. Wang, X. Xu, W. Yao, Topological mosaics in moiré superlattices of van der Waals heterobilayers. *Nat. Phys.* **13**, 356–362 (2017).
12. H. Yu, G.-B. Liu, J. Tang, X. Xu, W. Yao, Moiré excitons: From programmable quantum emitter arrays to spin-orbit-coupled artificial lattices. *Sci. Adv.* **3**, e1701696 (2017).
13. Y. Cao, V. Fatemi, S. Fang, K. Watanabe, T. Taniguchi, E. Kaxiras, P. Jarillo-Herrero, Unconventional superconductivity in magic-angle graphene superlattices. *Nature* **556**, 43–50 (2018).
14. Y. Cao, V. Fatemi, A. Demir, S. Fang, S. L. Tomarken, J. Y. Luo, J. D. Sanchez-Yamagishi, K. Watanabe, T. Taniguchi, E. Kaxiras, R. C. Ashoori, P. Jarillo-Herrero, Correlated insulator behaviour at half-filling in magic-angle graphene superlattices. *Nature* **556**, 80–84 (2018).
15. K. L. Seyler, P. Rivera, H. Yu, N. P. Wilson, E. L. Ray, D. G. Mandrus, J. Yan, W. Yao, X. Xu, Signatures of moiré-trapped valley excitons in $MoSe_2/WSe_2$ heterobilayers. *Nature* **567**, 66–70 (2019).
16. K. Tran, G. Moody, F. Wu, X. Lu, J. Choi, K. Kim, A. Rai, D. A. Sanchez, J. Quan, A. Singh, J. Embley, A. Zepeda, M. Campbell, T. Autry, T. Taniguchi, K. Watanabe, N. Lu, S. K. Banerjee, K. L. Silverman, S. Kim, E. Tutuc, L. Yang, A. H. MacDonald, X. Li, Evidence for moiré excitons in van der Waals heterostructures. *Nature* **567**, 71–75 (2019).
17. C. Jin, E. C. Regan, A. Yan, M. Iqbal Bakti Utama, D. Wang, S. Zhao, Y. Qin, S. Yang, Z. Zheng, S. Shi, K. Watanabe, T. Taniguchi, S. Tongay, A. Zettl, F. Wang, Observation of moiré excitons in WSe_2/WS_2 heterostructure superlattices. *Nature* **567**, 76–80 (2019).
18. E. M. Alexeev, D. A. Ruiz-Tijerina, M. Danovich, M. J. Hamer, D. J. Terry, P. K. Nayak, S. Ahn, S. Pak, J. Lee, J. I. Sohn, M. R. Molas, M. Koperski, K. Watanabe, T. Taniguchi, K. S. Novoselov, R. V. Gorbachev, H. S. Shin, V. I. Fal'ko, A. I. Tartakovskii, Resonantly hybridized excitons in moiré superlattices in van der Waals heterostructures. *Nature* **567**, 81–86 (2019).
19. N. R. Wilson, P. V. Nguyen, K. Seyler, P. Rivera, A. J. Marsden, Z. P. L. Laker, G. C. Constantinescu, V. Kandyba, A. Barinov, N. D. M. Hine, X. Xu, D. H. Cobden, Determination of band offsets, hybridization, and exciton binding in 2D semiconductor heterostructures. *Sci. Adv.* **3**, e1601832 (2017).
20. K. Liu, L. Zhang, T. Cao, C. Jin, D. Qiu, Q. Zhou, A. Zettl, P. Yang, S. G. Louie, F. Wang, Evolution of interlayer coupling in twisted molybdenum disulfide bilayers. *Nat. Commun.* **5**, 4966 (2014).
21. A. M. van der Zande, J. Kunstmann, A. Chernikov, D. A. Chenet, Y. You, X. Zhang, P. Y. Huang, T. C. Berkelbach, L. Wang, F. Zhang, M. S. Hybertsen, D. A. Muller, D. R. Reichman, T. F. Heinz, J. C. Hone, Tailoring the electronic structure in bilayer molybdenum disulfide via interlayer twist. *Nano Lett.* **14**, 3869–3875 (2014).
22. P.-C. Yeh, W. Jin, N. Zaki, J. Kunstmann, D. Chenet, G. Arefe, J. T. Sadowski, J. I. Dadap, P. Sutter, J. Hone, R. M. Osgood Jr., Direct measurement of the tunable electronic structure of bilayer MoS_2 by interlayer twist. *Nano Lett.* **16**, 953–959 (2016).
23. C. Zhang, C.-P. Chuu, X. Ren, M.-Y. Li, L.-J. Li, C. Jin, M.-Y. Chou, C.-K. Shih, Interlayer couplings, moiré patterns, and 2D electronic superlattices in MoS_2/WSe_2 hetero-bilayers. *Sci. Adv.* **3**, e1601459 (2017).
24. J. Kunstmann, F. Mooshammer, P. Nagler, A. Chaves, F. Stein, N. Paradiso, G. Plechinger, C. Strunk, C. Schüller, G. Seifert, D. R. Reichman, T. Korn, Momentum-space indirect interlayer excitons in transition-metal dichalcogenide van der Waals heterostructures. *Nat. Phys.* **14**, 801–805 (2018).
25. A. T. Hanbicki, H.-J. Chuang, M. R. Rosenberger, C. S. Hellberg, S. V. Sivaram, K. M. McCreary, I. I. Mazin, B. T. Jonker, Double indirect interlayer exciton in a $MoSe_2/WSe_2$ van der Waals heterostructure. *ACS Nano* **12**, 4719–4726 (2018).
26. D. Huang, E. Kaxiras, Electric field tuning of band offsets in transition metal dichalcogenides. *Phys. Rev. B.* **94**, 241303 (2016).
27. J.-K. Huang, J. Pu, C.-L. Hsu, M.-H. Chiu, Z.-Y. Juang, Y.-H. Chang, W.-H. Chang, Y. Iwasa, T. Takenobu, L.-J. Li, Large-area synthesis of highly crystalline WSe_2 monolayers and device applications. *ACS Nano* **8**, 923–930 (2014).
28. Y.-H. Chang, W. Zang, Y. Zhu, Y. Han, J. Pu, J.-K. Chang, W.-T. Hsu, J.-K. Huang, C.-L. Hsu, M.-H. Chiu, T. Takenobu, H. Li, C.-I. Wu, W.-H. Chang, A. T. S. Wee, L.-J. Li, Monolayer $MoSe_2$ grown by chemical vapor deposition for fast photodetection. *ACS Nano* **8**, 8582–8590 (2014).
29. W.-T. Hsu, Z.-A. Zhao, L.-J. Li, C.-H. Chen, M.-H. Chiu, P.-S. Chang, Y.-C. Chou, W.-H. Chang, Second harmonic generation from artificially stacked transition metal dichalcogenide twisted bilayers. *ACS Nano* **8**, 2951–2958 (2014).
30. B. L. Evans, R. A. Hazelwood, Optical and structural properties of $MoSe_2$. *Phys. Stat. Sol.* **4**, 181–192 (1971).
31. S. H. El-Mahalawy, B. L. Evans, The thermal expansion of 2H-MoS_2, 2H-$MoSe_2$ and 2H-WSe_2 between 20 and 800°C. *J. Appl. Cryst.* **9**, 403–406 (1976).
32. R. Murray, B. L. Evans, The thermal expansion of 2H-MoS_2 and 2H-WSe_2 between 10 and 320 K. *J. Appl. Cryst.* **12**, 312–315 (1979).
33. R. Schmidt, I. Niehues, R. Schneider, M. Drüppel, T. Deilmann, M. Rohlfing, S. Michaelis de Vasconcellos, A. Castellanos-Gomez, R. Bratschitsch, Reversible uniaxial strain tuning in atomically thin WSe_2. *2D Mater.* **3**, 021011 (2016).

Acknowledgments

Funding: This research was supported by grants from the Welch Foundation (F-1672), the NSF (DMR-1808751), the NSF MRSEC program (DMR-1720595), and the U.S. Air Force (FA2386-18-1-4097). W.-T.H. acknowledges the support from the Ministry of Science and Technology of Taiwan (MOST-107-2917-I-564-010). W.-H.C. acknowledges the support from the Ministry of Science and Technology of Taiwan (MOST-105-2119-M-009-014-MY3 and MOST-107-2112-M-009-024-MY3). W.Y. acknowledges the support from the Research Grants Council of HKSAR (HKU17312916). **Author contributions:** C.-K.S. and W.-T.H. conceived the idea and designed the experiment. W.-T.H. and B.-H.L. performed the spectroscopy measurements and analyses. The CVD samples were grown and characterized by L.-S.L. under the supervision of L.-J.L. and W.-H.C. M.-H.L., W.-T.H., and L.-S.L. performed the TEM measurements, assisted by M.-W.C. W.-T.H., W.-H.C., W.Y., and C.K.S. developed the model to interpret the spectroscopic data. C.K.S. and W.-T.H. wrote the paper, with key inputs from W.-H.C. and W.Y. All authors discussed the results and commented on the manuscript. **Competing interests:** The authors declare that they have no competing interests. **Data and materials availability:** All data needed to evaluate the conclusions in the paper are present in the paper and/or the Supplementary Materials. Additional data related to this paper may be requested from the authors.

Submitted 18 April 2019
Accepted 22 October 2019
Published 20 December 2019
10.1126/sciadv.aax7407

Citation: W.-T. Hsu, B.-H. Lin, L.-S. Lu, M.-H. Lee, M.-W. Chu, L.-J. Li, W. Yao, W.-H. Chang, C.-K. Shih, Tailoring excitonic states of van der Waals bilayers through stacking configuration, band alignment, and valley spin. *Sci. Adv.* **5**, eaax7407 (2019).

Science Advances

Tailoring excitonic states of van der Waals bilayers through stacking configuration, band alignment, and valley spin

Wei-Ting Hsu, Bo-Han Lin, Li-Syuan Lu, Ming-Hao Lee, Ming-Wen Chu, Lain-Jong Li, Wang Yao, Wen-Hao Chang and Chih-Kang Shih

Sci Adv **5** (12), eaax7407.
DOI: 10.1126/sciadv.aax7407

Science Advances (ISSN 2375-2548) is published by the American Association for the Advancement of Science, 1200 New York Avenue NW, Washington, DC 20005. The title *Science Advances* is a registered trademark of AAAS.